Matter and Radiation at Extremes

LETTER

pubs.aip.org/aip/mre

Editor's Pick

# Backward scattering of laser plasma interactions from hundreds-of-joules broadband laser on thick target

Cite as: Matter Radiat. Extremes 9, 015602 (2024); doi: 10.1063/5.0122406
Submitted: 24 August 2022 • Accepted: 16 October 2023 •
Published Online: 22 November 2023



Peipei Wang, Honghai An, Zhiheng Fang, Jun Xiong, Zhiyong Xie, Chen Wang,[a] Zhiyu He, Guo Jia, Ruirong Wang, Shu Zheng, Lan Xia, Wei Feng, Haitao Shi, Wei Wang, Jinren Sun, Yanqi Gao, and Sizu Fu

## AFFILIATIONS

Shanghai Institute of Laser Plasma, CAEP, Shanghai 201899, People's Republic of China

[a]**Author to whom correspondence should be addressed:** wch11@163.com and wangch@mail.shcnc.ac.cn

## ABSTRACT

The use of broadband laser technology is a novel approach for inhibiting processes related to laser plasma interactions (LPIs). In this study, several preliminary experiments into broadband-laser-driven LPIs are carried out using a newly established hundreds-of-joules broadband second-harmonic-generation laser facility. Through direct comparison with LPI results for a traditional narrowband laser, the actual LPI-suppression effect of the broadband laser is shown. The broadband laser had a clear suppressive effect on both back-stimulated Raman scattering and back-stimulated Brillouin scattering at laser intensities below $1 \times 10^{15}$ W cm$^{-2}$. An abnormal hot-electron phenomenon is also investigated, using targets of different thicknesses.



## I. INTRODUCTION

Laser plasma interactions (LPIs), particularly laser plasma instabilities, are important in laser plasma research, since they can determine the success or failure of inertial confinement fusion (ICF) ignition.[1–3] Hence, reducing the contributions of LPI-related processes [e.g., stimulated Brillouin scattering (SBS) and stimulated Raman scattering (SRS)] constitutes an essential research topic. To achieve this purpose, numerous theoretical and experimental studies have been performed over the past few decades.[1,4–12] These studies have usually relied on changing the state of the incident laser and plasma. One typical LPI-process-suppression strategy is the triple-frequency technique used to drive the laser in current ICF experiments.[1] For SRS and SBS, the LPI gain is proportional to the third power of the incident light wavelength. In other words, to reduce the harm caused by the LPI process, a driving laser source with a shorter wavelength and higher frequency is frequently employed. Thus, through technical improvements and repeated verification, the fundamental-frequency laser of the Cyclops laser (used in the laser device of the Lawrence Livermore National Laboratory in the USA) has been developed for the National Ignition Facility (NIF) and SGIII laser devices, which both adopt a triple-frequency laser driving technology. Alongside frequency doubling, various laser decoherence techniques have been adopted in laser experiment equipment, with the aim of reducing the spatial and temporal coherence of the laser and thereby suppressing LPIs. Many strategies have been proposed to suppress laser plasma instabilities, using laser smoothing techniques,[6–10] time profile shaping,[4] and enhanced plasma damping.[11,12] Several beam-smoothing techniques [e.g., continuous phase plates (CPPs)[6] and induced spatial incoherence (ISI)][10] have been developed. Laser plasma research is extremely challenging, owing to the interdependence of the plasma hydrodynamics and the laser-driven instabilities.[13] Although ignition has been achieved, research into higher gains and lower driving conditions remains an important next step. However, current progress in beam smoothing technology fails to satisfy the demands of this task. Hence, it is necessary to study laser plasma interaction in more detail.

Broadband lasers provide a possible option for restraining LPI processes. An increase in the laser bandwidth produces a decrease in its coherence. This may be attributable to a decrease in the effective light intensity of the plasma, which in turn may inhibit the occurrence and development of the related LPI processes.

The concept of broadband lasers was developed first. In 1974, Thomson and Karush[14] proposed the concept of using a limited bandwidth to suppress parameter instabilities. Later researchers continued this work on broadband lasers, demonstrating their possible inhibitory effects on LPI.[5–22] Through numerical simulations, Follett *et al.*[20,21] found that broadband lasers can suppress the double-plasma decay process and improve the threshold conditions for the development of absolute instabilities. However, these previous studies were primarily based on simulations. No convincing experimental reports on LPIs driven by high-energy broadband lasers have been published. Progress in the use of broadband lasers has long been limited by low overall output energies and insurmountable safety problems. The rapid technological developments in recent years, however, mean that some serious technical problems are expected to be resolved.

A broadband double-frequency laser facility with an output energy of hundreds of joules, operating on the basis of superluminescent diode (SLD) technology has constructed by researchers at the Shanghai Institute of Laser Plasma.[23,24] SLDs have been introduced into the ICF field as a lower-coherence seed source. Following a series of technological breakthroughs, this high-power laser facility now provides not only a verification platform for key techniques and the system integration of a low-coherence laser driver, but also a new type of experimental platform for research into LPI. Hence, to address the abovementioned shortcomings of research in this area, we conducted a preliminary experiment into laser-driven LPI scattering at this facility (referred to as Kunwu).

## II. BROADBAND LASER FACILITY

The incident laser can be either a broadband or narrowband second-harmonic generation laser with an output pulse width of a few nanoseconds and an energy of several hundred joules. The center wavelength and the bandwidth of the broadband laser are 529.5 and 3 nm, respectively. The temporal coherence is less than 300 fs. The facility also retains the output capabilities of the traditional narrowband laser, to ensure a broadband output of the same pulse width and energy. The center wavelength and bandwidth of the highly coherent narrowband laser are 526.5 and 0.3 nm, respectively. Figure 1 shows the laser parameters for a pulse width of 3 ns and an energy of 500 J, as measured in the experiment. Figure 1(a) shows the pulse waveforms of the broadband and narrowband lasers. There are slight differences between the two conditions. However, the overall shape is basically the same, indicating that the facility is consistent in terms of broad- and narrowband laser outputs. Figure 1(b) shows the integrated spectra of both lasers. A slight difference in central wavelength and a significant difference in bandwidth can be observed. The bandwidth of the narrowband laser is very narrow. The spectrum of the broadband laser exhibits a

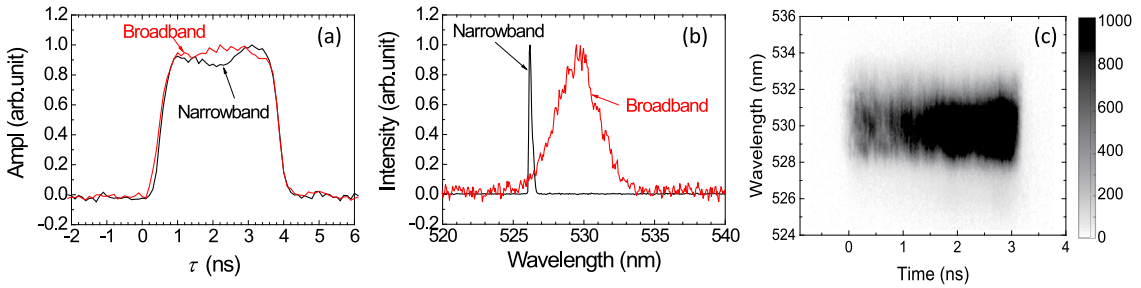


**FIG. 1.** Laser parameters of Kunwu lasers: (a) measured pulse waveform; (b) integral spectrum of broadband and narrowband lasers; (c) measured time spectral distribution of broadband laser.

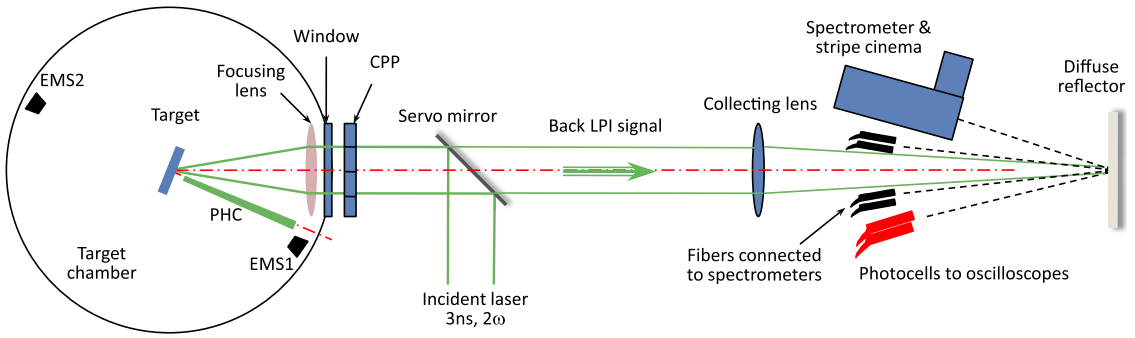


**FIG. 2.** Schematic of experimental setup.

clear triangular shape, and its full width at half maximum (FWHM) exceeds 3 nm. Figure 1(c) shows the time-resolved spectral distribution of the broadband laser, as measured using a spectrometer and streak camera. It can be clearly seen that under a change in pulse time, the broadband laser maintains a relatively wide spectrum with only minimal changes. This indicates that the Kunwu laser facility exhibits broadband characteristics throughout.

## III. EXPERIMENTAL DETAILS

The experiment in this study was conducted using a single-beam $2\omega$ laser with broadband or narrowband characteristics to drive a $C_8H_8$ plane-thick target. A broadband long-pulse (3 ns) laser initially ablated the target to generate plasma. Therefore, it continued to interact with the continuously generated plasma to trigger the occurrence and development of LPI-related processes. The thickness of the target was 300 $\mu$m, sufficient to avoid being burnt during the pulse cycle of the 3 ns laser. The experimental scheme is illustrated in Fig. 2. After focusing, the broadband or narrowband $2\omega$ laser beams entered the target chamber through the servo mirror and irradiated the $C_8H_8$ plane target. The generated LPI backscattered signals were recorded using various collection devices. In this study, we focused on the backscattering component of the LPIs. The generated backscattered LPI signal traveled backward along the optical path. It entered the diffuse reflector plate and was recorded by various acquisition devices after passing through a focusing mirror collimator, servo mirror, and collection lens. Reflected light might have appeared as noise if the incident laser reached the plane target and thereby entered the backscattered collection path. To prevent this, the normal direction of the target surface was set to deviate from that of the incident laser by ~10° in the horizontal direction. A continuous phase plate (CPP) was placed before the main focusing lens to obtain a uniform focal spot. The CPP used in this experiment included two design focal spot sizes of diameters 150 and 200 $\mu$m (referred to as 150CPP and 200CPP).

An x-ray pinhole camera was placed in front of the target chamber to monitor the laser focus. The pinhole camera was on the target surface normal, with a pinhole size of 10 $\mu$m and pinhole target distance of ~88 mm, to provide a magnification of ~6.4×. No filter was placed in front of the detector imaging plate (IP). Two sets of electron magnetic spectrometers (EMSs) were placed at ~5° normal to the target surface in front of and behind the target, to measure the energy spectrum of the outgoing hot electrons. The parameters of the two EMS sets were identical. The induction intensity was 0.3 T, the incident collimation hole diameter was 3 mm, the distance from the target surface was ~575 mm, and the measured energy spectrum range was 10–500 keV.

The use of a diffuse-reflected plate reflector (a flat plate with a special surface treatment) to measure the LPI scattering signal has been verified over many years and represents a conventional diagnostic technique for the NIF and elsewhere.[25]

By recording the diffusely reflected signal in a specific direction, the spectrum and energy of the incident beam, alongside other information, can be obtained after calibration and post-processing.

A variety of detectors were set up in front of the diffuse reflector, to measure the LPI-backscattered signal. The main detector was a combination of a fiber-optic probe and a spectrometer, which measured the time-integrated spectral signals of backscattered SBS (BSBS) and backscattered SRS (BSRS), respectively. In the experiment, the slit of the spectrometer was fully opened, and the slit width considerably exceeded the inner diameter of the optical fiber, to ensure that all scattered light signals collected by the optical fiber probe could be recorded.

For BSBS, a spectrometer consisting of a 2400 line/mm grating and visible-light charge-coupled device (CCD) with a pixel size of 20 × 20 $\mu m^2$ was selected for measurement. The center wavelength was 530 nm, and the corresponding spectral measurement range was ~520 to 540 nm. For BSRS, a spectrometer consisting of a 150 line/mm grating and a visible light CCD with a pixel size of 20 × 20 $\mu m^2$ was selected for measurement. The center wavelength was selected as 700–800 nm, and the corresponding spectral measurement range covered the 500–1100 nm band. This range includes a band at ~530 nm, where BSBS can be measured. Two limiting filters with a 532 nm central wavelength and 10 nm bandwidth were placed in front of the fiber-optic probe, to prevent saturation of the CCD count. Furthermore, the spectral resolution of the measurement was relatively low because of the large slit in the spectrometer.

Additionally, a system consisting of a photocell and oscilloscope was placed in front of the diffusion plate to measure the time characteristics of the backscattering data. The photocell was aimed at a light spot on the diffuse reflection plate. The scattered signals were collected. After proper filtering and attenuation, the signal was transmitted to an oscilloscope. Finally, a temporal waveform was obtained. The BSBS or BSRS data were obtained by placing different filters in front of different photocells. For BSBS, the filter consisted of two SP600 pieces and several grayscale ones. The SP600 ensured high transmittance of optical signals in the 400–600 nm band, whereas optical signals in other bands were attenuated. This was suitable for measuring the BSBS signals at wavelengths near 530 nm. For the BSRS, the filter consisted of two pieces of LP550 and several grayscale pieces. The LP550 ensured that the optical signal above 550 nm was highly transparent, whereas the optical signal below 550 nm was greatly attenuated. This ensured that the recorded signal was relatively clean.

The combination of a spectrometer and streak camera was also used to measure time-resolved spectral signals. The slit of the spectrometer was directed toward the light spot on the diffuse reflection plate. The slit of the streak camera was aimed directly at the spectral signal output of the spectrometer. Measurement of BSBS or BSRS could be realized by selecting different bands from the spectrograph.

## IV. EXPERIMENTAL RESULTS

### A. Focal spot image from pinhole camera

Figure 3 shows an x-ray image of the focal spots produced by laser irradiation of a planar thick target under different conditions. The images were captured using the pinhole camera. The $C_8H_8$ plane target was of thickness 300 $\mu$m. The pulse of the $2\omega$ lasers was a trapezoidal wave with a FWHM of ~3 ns. The energies of the $2\omega$ lasers were 400–500 J. Figures 3(a)–3(f) show images obtained under narrowband and broadband laser conditions, respectively.

Figures 3(a) and 3(d) show x-ray images of the focal spots under point-focusing conditions. The luminous images of the focal spots are relatively small, regardless of the bandwidth. The shapes are

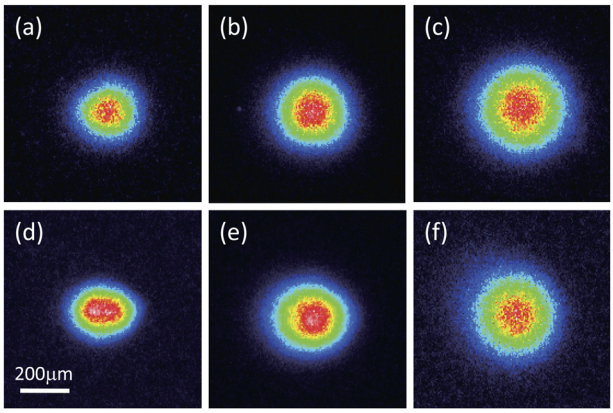


**FIG. 3.** X-ray images of focal spots under (a)–(c) narrowband and (d)–(f) broadband laser conditions. (a) and (d) Images under point-focusing conditions. (b) and (c) Images obtained with 150CPP. (c) and (f) Images obtained with 200CPP.

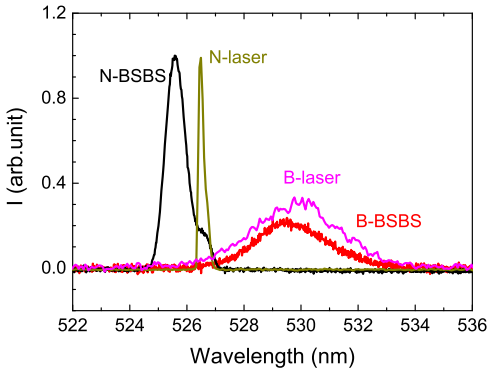


**FIG. 4.** Broadband and narrowband laser-driven BSBS integrated spectra and the spectra of the incident laser.

not circular. Moreover, factors such as shape and intensity distribution are very unstable. These factors differ for different shots. This is understandable for laser focal spots without beam-smoothing. Hence, the CPP technique was adopted. A more uniform focal spot was obtained by placing the CPP in front of the main focusing lens. Figures 3(b), 3(e), 3(c), and 3(f) show x-ray luminescence images of the measured spots. The focal spot for the CPP was far superior to that obtained under point focusing. The focal spot became more rounded and smoother. By contrast, the stability of the focal spots between different shots was significantly improved.

Figures 3(b) and 3(e) show the images obtained with 150CPP, where the scanning FWHM was 190 $\mu$m. Figures 3(c) and 3(f) show the images obtained with 200CPP, where the scanning FWHM was 230 $\mu$m. These values were slightly larger than the focal spot design values of the corresponding CPP. Before the experiment, the focal spot size of the CPP was tested using several methods, including optical signal debugging and tiny energy-ablating Al mirrors. The results indicate that the size of the focal spot is consistent with the design values. The x-ray pinhole camera image shows a larger luminous size, possibly attributable to the luminescence of the expanding plasma in the focal spot. The actual laser focal spot should be similar to the designed value. Therefore, we used the CPP design value to calculate the laser intensity.

In Fig. 3, it can be observed that the differences between the focal spots of the narrowband laser and those of the broadband laser are very small. Thus, little difference arises between the narrowband and broadband lasers in terms of the laser focus. Considering the instability of point focusing, subsequent experiments primarily used the CPP focus mode.

### B. Results for BSBS

Figure 4 shows two typical broadband and narrowband laser-driven BSBS-integrated spectra. The incident laser spectra are also shown. The intensities of the spectral lines along the $y$ axis have been appropriately adjusted to obtain a clearer display. The curves are not correlated with each other. The BSBS signals induced by broadband and narrowband lasers are completely different. This is primarily attributable to the difference in the driving laser spectrum. A small peak at the main laser wavelength (526.5 nm) and a large one at a shorter wavelength (525.5 nm) are observed for the narrowband laser. The small peak at 526.5 nm could correspond to the SBS component with an unchanged wavelength (which may contain a small amount of spurious environmental noise). Meanwhile, the peak at 525.5 nm should correspond to the blue-shifted BSBS signal, which may result from the Doppler effect produced by the expanding plasma. However, for the broadband laser, only a broad peak with a center at 529.5 nm is observed. The shape resembles that of the incident laser. In fact, a blue-shift phenomenon should also occur, as can be seen in the figure. However, the magnitude of the blue shift is less than the bandwidth of the broadband laser. Thus, it is difficult to distinguish between them.

Figure 5 shows the relationship between the BSBS energy ratio (with respect to the incident drive laser energy) and the laser intensity on the target surface. As mentioned above, the laser intensity on the target surface was calculated using the incident laser energy on the target, the pulse width, and the design value of the CPP. The experimental data points are distributed in the laser intensity range of (3–10) $\times$ $10^{14}$ W cm$^{-2}$. Different laser power densities can be achieved using different CPP sizes and incident laser energies.

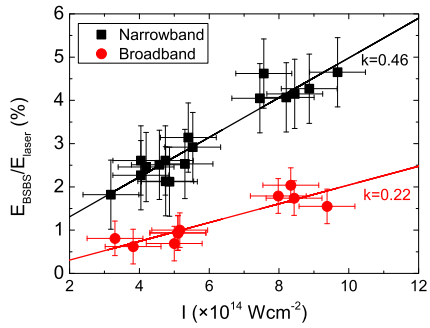


**FIG. 5.** Relationship between BSBS energy ratio and laser intensity on target surface.

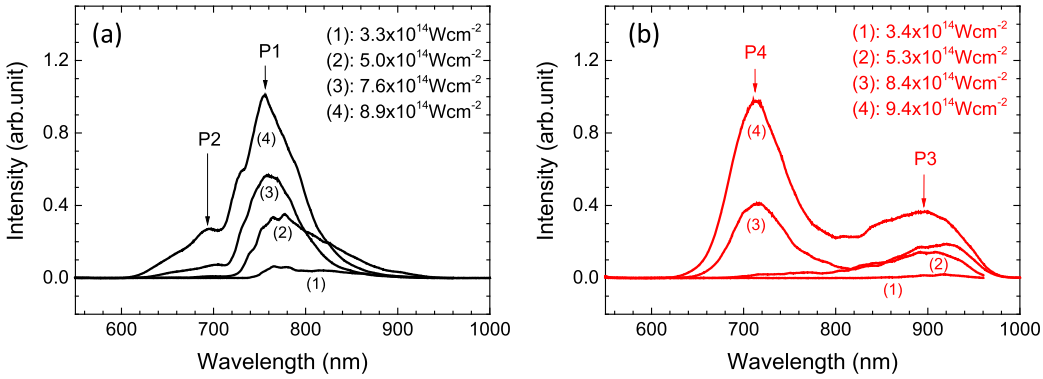


**FIG. 6.** Laser-driven BSRS integrated spectra at different laser intensities: (a) narrowband; (b) broadband.

Among these options, 200CPP was used for data with laser intensities below $6 \times 10^{14}$ Wcm$^{-2}$, and 150CPP was used for intensities exceeding $6 \times 10^{14}$ W cm$^{-2}$.

Figure 5 shows that the BSBS energy ratio of the broadband laser is much lower than that of the narrowband laser. Furthermore, the BSBS of both broadband and narrowband lasers increases as the laser intensity increases, which may indicate increasing laser plasma instabilities. The growth slope $k$ of the broadband laser is ~0.22, whereas that of the narrowband laser is ~0.46. The growth rate of the BSBS driven by the broadband laser is significantly lower than that driven by the narrowband laser (only one-third of that induced by the narrowband laser at the same laser intensity). To some extent, these results may prove the effectiveness of the broadband laser in suppressing BSBS.

### C. Results for BSRS

Figure 6 shows the results for the BSRS integral spectra of two typical broadband lasers and the normalized narrowband laser driving conditions. The BSRS signals of both the narrowband and broadband lasers present a bimodal distribution and are directly related to the laser intensity. Under narrowband laser conditions, the double peaks are marked as P1 and P2, with corresponding wavelengths ~750 and 680 nm, respectively. Figure 6(a) shows that the BSRS signal starts from a P1 single peak. With an increase in laser intensity, the intensity of the BSRS gradually increases and develops another peak, P2. The broadband double peaks are marked as P3 and P4, with corresponding wavelengths 900 and 710 nm, respectively. Figure 6(b) shows that the BSRS signal starts from the P3 single peak. With an increase in laser intensity, the intensity of the BSRS gradually increases and develops another peak, P4. Expressed in another way, for both narrowband and broadband conditions, only long-wavelength peaks (P1 and P3) appear when the laser intensity is low. Short-wavelength peaks (P2 and P4) gradually appear and are strengthened when the laser intensity is increased. However, there are clear differences between the narrowband and broadband conditions. First, the wavelengths of the two peaks for both conditions are different. Second, the increase in P2 (narrowband condition) is limited and still significantly lower than that in P1. However, the increase in P4 (broadband condition) is significant, and the intensity of P4 exceeds that of P3. Although the presence and intensity of the double peaks varies with changes in laser intensity, the positions of the double peaks remain almost unchanged. The BSRS spectrum shape is closely related to the plasma state (i.e., the electron density and electron temperature). Therefore, the shape of the BSRS spectrum, particularly the peak position, with the broadband laser differs significantly from that with the traditional narrowband laser.

In light of this, the time characteristics of this phenomenon were measured. Figure 7 shows the measurement results of the spectrometer and streak camera. Figure 7(a) shows that the P1 peak (with a wavelength of ~750 nm) first develops and runs through the entire laser pulse period of the narrowband laser. At a later stage of pulse development, the P2 peak at 680 nm begins to develop and gradually increases. However, for the broadband driving condition shown in Fig. 7(b), only a group of short-duration peaks are present in the image. Based on the spectral position and duration, this peak can be considered to correspond to the P4 peak, with a peak wavelength of ~710 nm. The P3 peak with a wavelength of ~900 nm is not observed. The wavelength of the P3 peak at 900 nm is beyond the response band of the streak camera used in the experiment. However, the development of the P3 peak is insufficient and the intensity is too low. In contrast to narrowband driving conditions, it is reasonable to assume that the P3 peak develops first and throughout the pulse cycle. Subsequently, the P4 peak gradually develops and rapidly exceeds the P3 peak in the later pulse period.

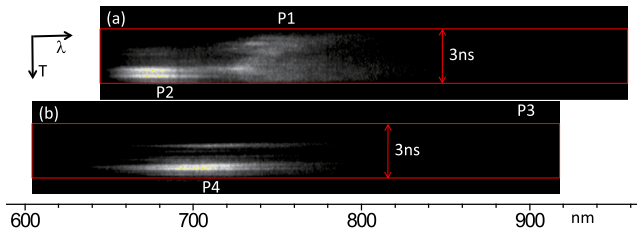


**FIG. 7.** Time-resolved spectral resolution signals of BSRS at laser intensity $9 \times 10^{14}$ W cm$^{-2}$, as measured by spectrometers and streak cameras: (a) narrowband; (b) broadband.

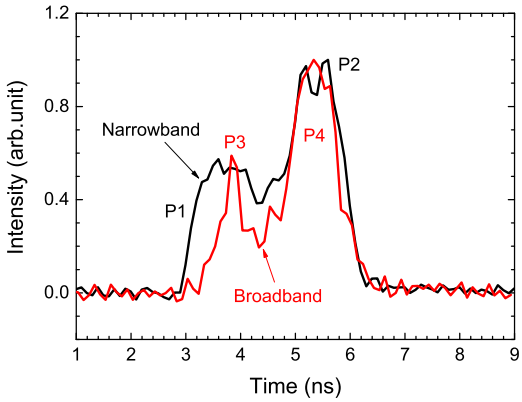


**FIG. 8.** Time-resolved spectral integral signals of BSRS, as measured by photocell and oscilloscope.

Figure 8 shows the measurements of the BSRS signal obtained using a system consisting of a photocell and an oscilloscope. The results have been normalized. This finding supports our previous conclusions. As shown in Fig. 8, the early peak P3 is very narrow and not fully developed under broadband laser conditions. The overall intensity is very weak.

The relationship between the BSRS energy ratio and the laser intensity on the target surface in the experiment is shown in Fig. 9. Compared with BSBS, the energy ratio of BSRS is much lower, as can be seen in the figure. Most of the BSRS values corresponding to the broadband laser are significantly lower than those corresponding to the narrowband laser. The BSRS under narrowband laser conditions increases linearly with increasing laser intensity, indicating that the current laser intensity does not satisfy the conditions of a nonlinear increase. The BSRS under broadband laser conditions also increases with increasing laser intensity. However, their growth trends are significantly different. It can be observed from the fitted curve that the change in the energy share with respect to the laser intensity is closer to an exponential distribution. This suggests that under broadband conditions, the BSRS increases more rapidly. With a further increase in the laser intensity, the broadband laser-driven SRS becomes stronger.

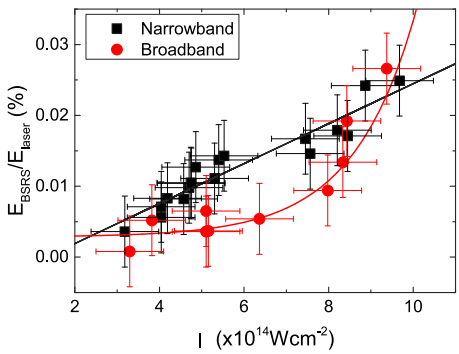


**FIG. 9.** Relationship between energy ratio of BSRS and laser intensity on target surface.

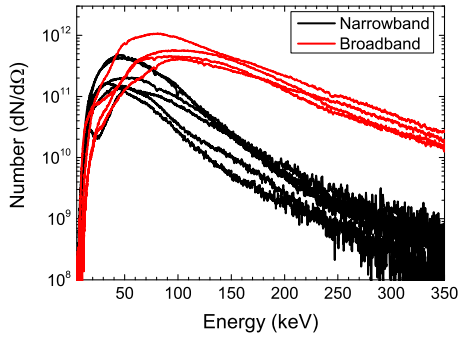


**FIG. 10.** Energy spectrum of hot electrons in front of the target under broadband and narrowband laser conditions from different shots at the same laser intensity.

### D. Results for hot electrons

The generation of hot electrons is another important aspect of LPI research. Two sets of EMSs were used to identify the hot electrons that escaped before and after the laser-driven target. As shown in Fig. 2, the two sets of EMS are identical, and their positions are rotationally symmetric with respect to the target position.

Figure 10 shows typical energy spectra of hot electrons in front of the target under broadband and narrowband laser driving conditions, as measured by EMS1. The figure shows data from several shots. It can be clearly seen that the energy spectrum of hot electrons under broadband conditions considerably exceeds that under narrowband conditions. This manifested in two ways: first, the electron number for the broadband laser is 1–2 orders of magnitude higher than that for the narrowband laser in the high-energy region (i.e., $E \geq 150$ keV); second, there is a difference in the peak position. It appears that the peak of the hot-electron energy spectrum under the broadband laser is higher, reaching ~100 keV. The peak position of the narrowband laser is ~50 keV. Furthermore, the hot-electron energy spectrum corresponding to the broadband laser is wider than that corresponding to the narrowband laser.

Figure 11 shows the relationship between the energy values of (a) the backward hot electrons (in front of the target, as measured by EMS1) and (b) the forward hot electrons (behind the target, as measured by EMS2), as well as the laser intensity at the position of the EMS. The energy of hot electrons in the solid angle of the broadband laser exceeds that of the narrowband laser in most situations, regardless of placement in front of or behind the target. This is an abnormal phenomenon, and it conflicts with the traditional perception that hot electrons are mainly derived from SRS. As mentioned above, the BSRS induced by the broadband laser is significantly weaker than that obtained under narrowband conditions in our experiment. This result indicates that BSRS is not the main source of hot electrons here. Thus, other mechanisms must induce the formation of hot electrons.

## V. ANALYSIS AND DISCUSSION

### A. Brief analysis for broadband laser

The LPI driven by the SLD-based broadband laser clearly differs from that driven by the traditional narrowband laser. The root

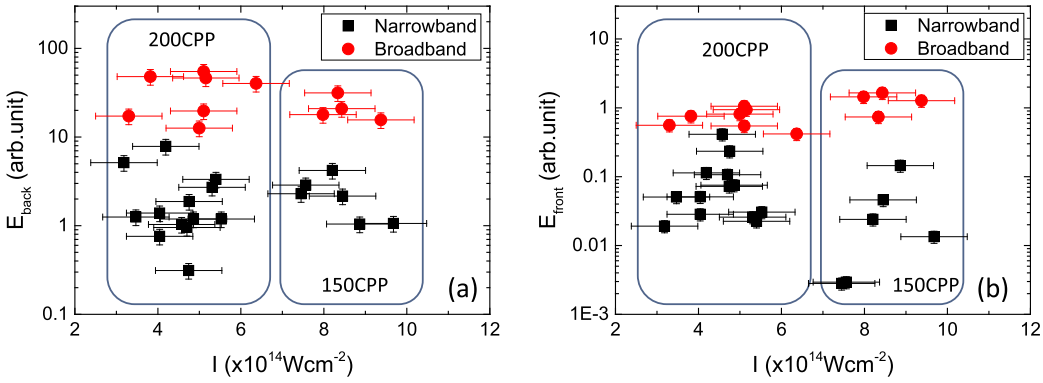


**FIG. 11.** Relationship between energy share of hot electrons and laser intensity (a) behind and (b) in front of the target.

cause is a decrease in coherence, caused by the increase in bandwidth. From a macroscopic point of view, this is equivalent to beam smoothing. A decrease in coherence indicates a decrease in the effective electric field intensity in the plasma. The LPI is directly related to the electric field intensity, and hence the LPI is somewhat reduced.

When traversing the plasma, incident light waves may excite ion acoustic waves (IAWs) or electron plasma waves (EPWs) and produce scattered light waves. These three waves—incident light waves, scattered light waves, and IAWs or EPWs—interact to produce different LPI processes. When the phase matching condition between the three waves is satisfied, resonance phenomena occur, and an unstable positive feedback loop is formed; this in turn considerably increases the scattering efficiency.

SBS is the elastic backscattering of incident photons on the IAWs. In general, SBS can occur in all regions where the electron density is below critical density (i.e., no significant resonance feedback processes occur). From this perspective, broadband lasers cannot exert a substantial influence on the development process of SBS compared with narrowband ones. The weaker SBS under broadband conditions is mainly attributable to the low coherence and lower effective electric field intensity produced by the broadband laser.

The SRS results are significantly different. SRS is the elastic scattering of the incident laser on the EPWs. Coherent feedback is generated when the incident light wave, electron plasma wave, and scattered light wave satisfy the resonance conditions. This significantly increases the intensity of the SRS. For a broadband laser, an increase in the bandwidth widens the wave vector distribution, which makes it possible to satisfy the resonance conditions over a wider range. As shown in Fig. 9, the SRS intensity decreases under a low laser intensity, which is consistent with the abovementioned SBS effect. That is, the low coherence and lower effective electric field intensity produced by the broadband laser lead to a decrease in the broadband laser-driven SRS. However, with an increase in laser intensity, a resonance effect gradually arises between the three waves. Through coherent feedback, the intensity of the SRS increases substantially and quickly exceeds that of the narrowband laser. Nevertheless, broadband lasers have different characteristics from traditional narrowband lasers. Thus, it remains possible to retain SRS by developing relevant techniques, on the basis of these characteristics.

### B. Abnormal phenomenon of hot electrons

The hot-electron anomalies are a matter of great concern. Traditionally, hot electrons originate from the Landau damping or plasma wave breakup caused by abnormal absorption; this may have a more direct correlation with the SRS. In our experiment, the BSRS was typically weaker than that for narrowband lasers, as discussed in Sec. IV C. However, in terms of hot electrons, broadband lasers offer a significant increase compared with narrowband lasers, in contrast to the BSRS results.

In addition, according to the current driving laser conditions (below $10^{15}$ W cm$^{-2}$), the energy of hot electrons usually varies from a few keV to tens of keV, which is consistent with the results shown for narrowband laser conditions in Fig. 11. However, in the case of broadband conditions, the peak energy reaches ~100 keV, in contrast to the traditional understanding. Therefore, it is suspected that the hot electrons in this experiment did not originate from SRS.

Four main mechanisms represent the dominant sources of hot electrons in laser plasma interactions: SRS, two-plasmon decay (TPD), resonance absorption, and parametric decay instability. Clear differences arise between the corresponding conditions. Therefore, we designed a novel experiment to investigate this phenomenon. This scheme is the same as that illustrated in Fig. 2.

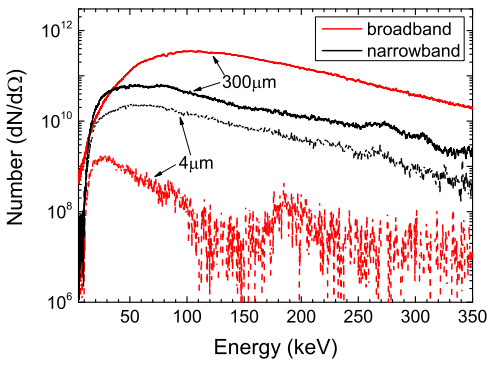


**FIG. 12.** Hot-electron energy spectra for different target thicknesses in front of the target.

However, the $C_8H_8$ plane target used in this experiment had two thicknesses: 4 and 300 $\mu$m. Furthermore, a point-focusing method was used.

Figure 12 shows the corresponding results for the backward hot electrons (in front of the target, as measured by EMS1). The four curves correspond to broadband thick, broadband thin, narrowband thick, and narrowband thin targets. The corresponding conditions for the four shots were similar. The pulse width of the driving laser was ~3 ns and the energy was ~400 J. It can be seen from the figure that the results for a thin target of 4 $\mu$m and a thick target of 300 $\mu$m were completely different. For a thin target of 4 $\mu$m, the energy of hot electrons under broadband conditions is significantly lower than that under narrowband conditions, which is consistent with the previous finding that hot electrons are mainly derived from SRS. For the 300 μm-thick target, the energy spectra of the hot electrons is greatly improved under broadband conditions. This trend matches that mentioned above.

In the experiment, the largest difference between the thin and thick targets should originate from the critical density surface of the plasma. For a thin target of 4 $\mu$m, the nanosecond driving laser can quickly burn through the material, and the plasma expands to the outside. During this process, the critical density $n_c$ surface is eliminated. On the other hand, for a thick target of 300 $\mu$m, the nanosecond driving laser cannot burn completely through the material. A critically dense surface is present near the target surface. Therefore, for the experiment with the 300 μm-thick target, the abnormal hot electrons under broadband laser driving conditions may be attributable to the existence of a critical density surface.

We reconsidered mechanisms besides SRS that may produce hot electrons. TPD mainly induces an electron density around near-quarter-critical density ($0.25n_c$). Thus, it may not be the source of the large increase in the number of hot electrons under broadband conditions. Resonance absorption occurs primarily near the critical density. However, the conditions under which resonant absorption occurs are stringent; this absorption requires a higher laser intensity and a larger oblique incidence angle. In this experiment, the laser intensity was only several $10^{14}$ W cm$^{-2}$, and the laser incident angle was only ~10°. Thus, resonance absorption is unlikely to be the source of the large increase in the number of hot electrons under broadband conditions. In addition, the dominant source of hot electrons was the parametric decay instability; this occurs when an incident photon decays into an IAW or EPW. The energy of the photons is mainly transferred to the EPW, which drives the generation of hot electrons. A characteristic of the parametric decay instability is that hot electrons can be excited in both the forward and backward directions, which is consistent with the experimental results.

However, it remains worthwhile studying why the parametric decay instability under broadband laser conditions exceeds that under narrowband laser conditions. It is conceivable that these phenomena are caused by the characteristics of broadband lasers. New experiments and targeted analytical simulations should be conducted in future research, to better understand the meaning and value of broadband lasers.

### C. Near-backward scattering

Near-backward scattering is also of interest in LPI research. It is generally believed that in the near-backward direction, the intensities of the SBS, SRS, and other LPIs decrease rapidly with increasing deviation angle from the back direction. In the experiments, the optical fiber probe was placed 15° and 25° away from the back and 80° from the tangent to the target plane. Thus, the near-backward and lateral scattering signals could be measured using a spectrometer. Figure 13 shows typical lateral LPI spectral information, as measured using the lateral optical fiber probe. The corresponding detection angle was 25°. The spectrum contains an SBS signal of wavelength ~530 nm and an SRS signal with a wavelength in the range of 600–1000 nm. It can be clearly seen from the figure that the intensity of SBS considerably exceeds that of SRS. Based on the peak intensity alone, SBS is ~500× stronger than SRS. Even though SRS occupies a relatively large wavelength range, the scattered energy contained in SRS is considerably less than that contained in SBS.

Figure 14 shows the energy information of SBS under different scattering measurement angles for the two shots. Although fluctuations can be observed in the data for the two shots, they still exhibit the same trend under both broadband and narrowband conditions. These results are consistent with expectations, and the SBS intensity decreases rapidly with increasing measurement

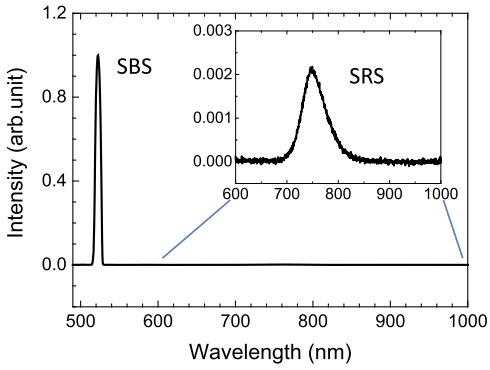


**FIG. 13.** Typical lateral LPI spectral information, as measured by lateral optical fiber probe, containing a strong SBS peak and a very weak SRS signal. The corresponding detection angle was 25°.

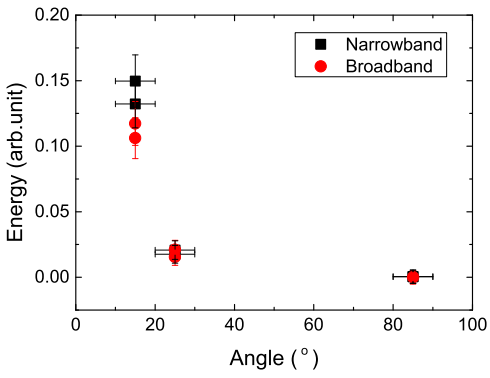


**FIG. 14.** Energy information of SBS at different scattering measurement angles.

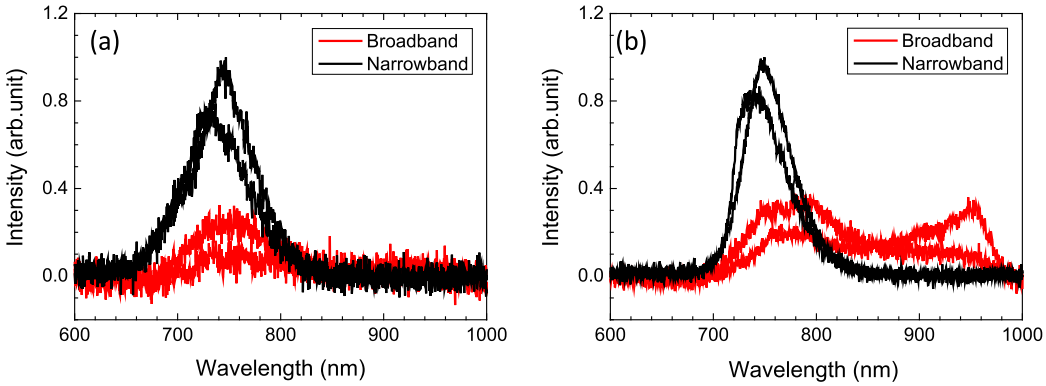


**FIG. 15.** SRS spectrum in (a) the 15° and (b) the 25° directions.

angle. The SBS intensity produced by the broadband laser is significantly lower than that produced by the narrowband laser at smaller angles (e.g., 15°). The average reduction is ~20%. However, with increasing angle, the SBS intensity produced by both broadband and narrowband lasers is fairly high (e.g., at 25°). Furthermore, the SBS intensities of both decrease substantially (approaching close to zero) when the position is 80° with respect to the tangent of the target plane.

Although the near-backward SRS is much weaker than the SBS, a significant difference remains at different measurement angles. Figure 15 shows the SRS spectra in (a) the 15° and (b) the 25° directions. The SRS spectra at the two positions are essentially identical for the narrowband laser. They exhibit a single-peak structure with a wavelength of ~750 nm. For the broadband condition, an evident difference is noticeable. There is again a unimodal structure at a wavelength of ~750 nm in the 15° direction, although the intensity is much weaker than under narrowband conditions. In the 25° direction, however, a bimodal structure with peak wavelengths of 760 and 950 nm is observed. This result can also be compared with the spectral distribution of the BSRS (shown in Fig. 6). For the narrowband condition, the peak at 750 nm resembles that of P1 in Fig. 6. P2 is not shown, because the signal was too weak. For the broadband condition, the 750 nm peak corresponds to P4, as shown in Fig. 6. P3 appears only in the 25° direction. However, the corresponding peak wavelengths are red-shifted compared to those of P3 and P4, as shown in Fig. 6. This may indicate that a clear physical phenomenon is involved, which is related to the possible wave-vector resonance matching produced by the broadband laser in different angular directions. This topic requires further analysis and research.

## VI. CONCLUSION

A preliminary experimental study of broadband laser-driven LPIs was conducted using a broadband SHG laser. Through a comparison with the results for a traditional narrowband laser under the same parameter conditions, we initially determined that the broadband laser had a clear suppressive effect on both BSBS and BSRS under a laser intensity of less than $1 \times 10^{15}$ W cm$^{-2}$. With increasing laser intensity, both BSBS and BSRS made a lower contribution and exhibited a slower increase. An abnormality in the hot-electron energy spectrum was observed under broadband laser driving, possibly attributable to the fact that a broadband laser is more likely to induce parametric decay instabilities. Finally, it should be noted that as a new low-coherence driver, this broadband laser differs significantly from traditional narrowband laser drivers. The results presented here reflect the contributions of broadband lasers in suppressing LPI-related processes, which may provide a basis for improving fundamental understanding of broadband lasers, as well as developing an in-depth understanding of LPIs.

## ACKNOWLEDGMENTS

This work was supported by the National Science Foundation of China under Award Nos. 12074353 and 12075227.

## AUTHOR DECLARATIONS

### Conflict of Interest

The authors have no conflicts to disclose.

### Author Contributions

**Peipei Wang**: Formal analysis (equal); Writing – original draft (equal); Writing – review & editing (equal). **Honghai An**: Data curation (equal); Formal analysis (equal). **Zhiheng Fang**: Data curation (equal); Formal analysis (equal). **Jun Xiong**: Data curation (equal); Formal analysis (equal). **Zhiyong Xie**: Data curation (equal); Formal analysis (equal). **Chen Wang**: Conceptualization (equal); Writing – original draft (equal). **Zhiyu He**: Data curation (equal); Formal analysis (equal). **Guo Jia**: Data curation (equal); Investigation (equal). **Ruirong Wang**: Investigation (equal); Methodology (equal). **Shu Zheng**: Investigation (equal). **Lan Xia**: Data curation (equal). **Wei Feng**: Data curation (equal). **Haitao Shi**: Data curation (equal). **Wei Wang**: Conceptualization (equal); Methodology (equal). **Jinren**

**Sun**: Methodology (equal); Validation (equal). **Yanqi Gao**: Methodology (equal). **Sizu Fu**: Conceptualization (equal); Methodology (equal).

## DATA AVAILABILITY

The data that support the findings of this study are available from the corresponding author upon reasonable request.

## REFERENCES


[1]J. D. Lindl, P. Amendt, R. L. Berger, S. G. Glendinning, S. H. Glenzer, S. W. Haan, R. L. Kauffman, O. L. Landen, and L. J. Suter, "The physics basis for ignition using indirect-drive targets on the National Ignition Facility," Phys. Plasmas **11**, 339 (2004).

[2]D. H. Froula, L. Divol, R. A. London, R. L. Berger, T. Döppner, N. B. Meezan, J. Ralph, J. S. Ross, L. J. Suter, and S. H. Glenzer, "Experimental basis for laser-plasma interactions in ignition hohlraums at the National Ignition Facility," Phys. Plasmas **17**, 056302 (2010).

[3]D. E. Hinkel, M. D. Rosen, E. A. Williams, A. B. Langdon, C. H. Still, D. A. Callahan, J. D. Moody, P. A. Michel, R. P. J. Town, R. A. London, and S. H. Langer, "Stimulated Raman scatter analyses of experiments conducted at the National Ignition Facility," Phys. Plasmas **18**, 056312 (2011).

[4]B. J. Albright, L. Yin, and B. Afeyan, "Control of stimulated Raman scattering in the strongly nonlinear and kinetic regime using spike trains of uneven duration and delay," Phys. Rev. Lett. **113**, 045002 (2014).

[5]D. Yang, Z. Li, S. W. Li, L. Hao, X. Li, L. Guo, S. Zou, X. Jiang, X. S. Peng, T. Xu, Y. Li, C. Y. Zheng, H. Cai, Z. Liu, J. Zheng, T. Gong, Z. Wang, H. Li, L. Kuang, Q. Li, F. Wang, S. Liu, J. Yang, S. Jiang, B. Zhang, and Y. Ding, "Laser plasma instability in indirect-drive inertial confinement fusion," Sci. Sin. Phys., Mech. Astron. **48**, 065203 (2018).

[6]S. N. Dixit, M. D. Feit, M. D. Perry, and H. T. Powell, "Designing fully continuous phase screens for tailoring focal-plane irradiance profiles," Opt. Lett. **21**, 1715 (1996).

[7]G. Cao, P. Shi, X. Zhang, R. Wu, S. Zhou, and Y. Li, "Improvement of target irradiation uniformity using spectral dispersion and distributed phase plate," Chin. J. Lasers **38**, 1002006 (2011).

[8]S. Skupsky, R. W. Short, T. Kessler, R. S. Craxton, S. Letzring, and J. M. Soures, "Improved laser-beam uniformity using the angular dispersion of frequency-modulated light," J. Appl. Phys. **66**, 3456 (1989).

[9]E. Lefebvre, R. L. Berger, A. B. Langdon, B. J. MacGowan, J. E. Rothenberg, and E. A. Williams, "Reduction of laser self-focusing in plasma by polarization smoothing," Phys. Plasmas **5**, 2701 (1998).

[10]J. Grun, M. H. Emery, C. K. Manka, T. N. Lee, E. A. Mclean, A. Mostovych, J. Stamper, S. Bodner *et al.*, "Rayleigh-Taylor instability growth rates in targets accelerated with a laser beam smoothed by induced spatial incoherence," Phys. Rev. Lett. **58**, 2672 (1987).

[11]C. J. McKinstrie, R. E. Giacone, and E. A. Startsev, "Accurate formulas for the Landau damping rates of electrostatic waves," Phys. Plasmas **6**, 463 (1999).

[12]P. Neumayer, R. L. Berger, L. Divol, D. H. Froula, R. A. London, B. J. MacGowan, N. B. Meezan, J. S. Ross, C. Sorce, L. J. Suter, and S. H. Glenzer, "Suppression of stimulated Brillouin scattering by increased Landau damping in multiple-ion-species hohlraum plasmas," Phys. Rev. Lett. **100**, 105001 (2008).

[13]E. M. Campbell, T. C. Sangster, V. N. Goncharov, J. D. Zuegel, S. F. B. Morse, C. Sorce, G. W. Collins, M. S. Wei, R. Betti, S. P. Regan, D. H. Froula, C. Dorrer, D. R. Harding, V. Gopalaswamy, J. P. Knauer, R. Shah, O. M. Mannion, J. A. Marozas, P. B. Radha, M. J. Rosenberg, T. J. B. Collins, A. R. Christopherson, A. A. Solodov, D. Cao, J. P. Palastro, R. K. Follett, and M. Farrell, "Direct-drive laser fusion: Status, plans and future," Philos. Trans. R. Soc., A **379**(2189), 20200011 (2021).

[14]J. J. Thomson and J. I. Karush, "Effects of finite-bandwidth driver on the parametric instability," Phys. Fluids **17**, 1608 (1974).

[15]P. N. Guzdar, C. S. Liu, and R. H. Lehmberg, "The effect of bandwidth on the convective Raman instability in inhomogeneous plasmas," Phys. Fluids B **3**, 2882 (1991).

[16]Y. Zhao, S. M. Weng, M. Chen, J. Zheng, H. B. Zhuo, C. Ren, Z. M. Sheng, and J. Zhang, "Effective suppression of parametric instabilities with decoupled broadband lasers in plasma," Phys. Plasmas **24**, 112102 (2017).

[17]Y. Zhao, S. Weng, Z. M. Sheng, and J. Q. Zhu, "Suppression of parametric instabilities in inhomogeneous plasma with multi-frequency light," Plasma Phys. Controlled Fusion **61**, 115008 (2019).

[18]H. Y. Zhou, C. Z. Xiao, D. B. Zou, X. Z. Li, Y. Yin, F. Q. Shao, and H. B. Zhuo, "Numerical study of bandwidth effect on stimulated Raman backscattering in nonlinear regime," Phys. Plasmas **25**, 062703 (2018).

[19]H. Y. Zhou, C. Z. Xiao, J. L. Jiao, Y. Lang, N. Zhao, D. Xie, D. B. Zou, Y. Yin, F. Q. Shao, and H. B. Zhuo, "Kinetic simulation of nonlinear stimulated Raman scattering excited by a rotated polarized pump," Plasma Phys. Controlled Fusion **61**, 105004 (2019).

[20]R. K. Follett, J. G. Shaw, J. F. Myatt, C. Dorrer, D. H. Froula, and J. P. Palastro, "Thresholds of absolute instabilities driven by a broadband laser," Phys. Plasmas **26**, 062111 (2019).

[21]R. K. Follett, J. G. Shaw, J. F. Myatt, J. P. Palastro, R. W. Short, and D. H. Froula, "Suppressing two-plasmon decay with laser frequency detuning," Phys. Rev. Lett. **120**, 135005 (2018).

[22]S. P. Obenschain, N. C. Luhmann, and P. T. Greiling, "Effects of finite-bandwidth driver pumps on the parametric-decay instability," Phys. Rev. Lett. **36**, 1309 (1976).

[23]Y. Q. Gao, Y. Cui, L. L. Ji, D. X. Rao, X. H. Zhao, F. J. Li, D. Liu, W. Feng, L. Xia, J. N. Liu, H. T. Shi, P. Y. Du, J. Liu, X. L. Li, T. Wang, T. X. Zhang, C. Shan, Y. L. Hua, W. X. Ma, X. Sun, X. F. Chen, X. G. Huang, J. Zhu, W. B. Pei, Z. Sui, and S. Z. Fu, "Development of low-coherence high-power laser drivers for inertial confinement fusion," Matter Radiat. Extremes **5**, 065201 (2020).

[24]Y. Cui, Y.Q. Gao, D.X. Rao, D. Liu, F.J. Li, L.L. Ji, H.T. Shi, J.N. Liu, X.H. Zhao, W. Feng, L. Xia, J. Liu, X.L. Li, T. Wang, W.X. Ma, and Z. Sui, "High-energy low-temporal-coherence instantaneous broadband pulse system," Opl. Lett. **44**, 2859 (2019).

[25]J. D. Moody, P. Datte, K. Krauter, E. Bond, P. A. Michel, S. H. Glenzer, L. Divol, C. Niemann, L. Suter, N. Meezan, B. J. MacGowan, R. Hibbard, R. London, J. Kilkenny, R. Wallace, J. L. Kline, K. Knittel, G. Frieders, B. Golick, G. Ross, K. Widmann, J. Jackson, S. Vernon, and T. Clancy, "Backscatter measurements for NIF ignition targets (invited)," Rev. Sci. Instrum. **81**, 10D921 (2010).